

TOMASZ JANOSZEK ^{1*}

NUMERICAL SIMULATION OF METHANE DISTRIBUTION AT THE LONGWALL WORKING WITH VARIOUS STAGES OF SHEARER ADVANCE

The article presents a methodology for predicting the impact of the longwall shearer's control parameter on methane emission rate to the working of a longwall based on computational fluid dynamics (CFD) methods. The methodology was applied to the

Z-11a longwall panel conditions at the Jankowice Hard Coal Mine. The results of the methane emissions rate in the working of a longwall for three variations of the position of the longwall shearer are shown and discussed. The modelled issue's geometry, numerical grid, assumptions, and boundary conditions are presented. The filtration parameters of goafs are discussed. Relationships to estimate the various sources of methane emissions into the air flowing around the longwall panel Z-11a are presented. The results of the model tests were compared with the mining data in the Z-11a longwall panel at the Jankowice Hard Coal Mine.

Keywords: Coal mine; longwall shearer operation; methane; ventilation; numerical model; computational fluid dynamics (CFD)

1. Introduction

Modern coal mine ventilation systems are becoming more complex due to the extensive network of underground excavations, which makes it challenging to predict the airflow due to fluctuations in aerodynamic potential, caused by the operation of fans. The acceptable values of methane concentration in the independent air stream might be exceeded in a very short time [6,7]. Computer approaches that solve equations representing fluid movement in a given geometry make it easier to analyse methane flow behaviour in the longwall panel, especially during the

¹ CENTRAL MINING INSTITUTE – NATIONAL RESEARCH INSTITUTE (GIG-PIB), PLAC GWARKÓW 1, 40-166 KATOWICE, POLAND

* Corresponding author: tjanoszek@gig.eu



© 2024. The Author(s). This is an open-access article distributed under the terms of the Creative Commons Attribution-NonCommercial License (CC BY-NC 4.0, <https://creativecommons.org/licenses/by-nc/4.0/deed.en>) which permits the use, redistribution of the material in any medium or format, transforming and building upon the material, provided that the article is properly cited, the use is non-commercial, and no modifications or adaptations are made.

design phase of operations [25]. The concepts of modelling methane emission into the longwall working are contained in the reflection of fluid transport equations, physical phenomenon models, and turbulence models [2,11,13-17].

The influence of the shearer's position on the methane emissions rate in the longwall working has not yet been studied in the literature, using 3D numerical modelling. Dziurzyński et al. in [4] presented the result of the influence of the operation of a longwall shearer and conveyors on emissions and the migration of methane into the longwall working. The results were obtained from 2D modelling and compared with the mining data in longwall panels 841A and 841B at the Bielszowice Hard Coal Mine. Koptoń in [9] described the mechanism of methane emission from the longwall coal face into the working of a longwall in the form of a mathematical model, taking into account the sorption properties of coal. The author used 2D numerical modelling to simulate the longwall coal face destruction as a function of the compressive strength of the roof rocks. Nguyen et al. [18] presented a methodology for predicting the absolute methane emission rate based on the determination of destressing zones generated by longwall mining operations, using 2D rock mass modelling.

Juganda et al. [8] presented a hybrid approach to modelling gas flows in and through the gob under methane hazard conditions during the longwall panel operations using the computational fluid dynamics (CFD) method. Juganda et al. [9] developed CFD models that may be used to analyse the effects of methane gas explosions on mine ventilation and are capable of simulating large-scale explosions in longwall mines. To simulate methane gas explosions caused by face ignition when the coal face is being sheared. Tutak et al. [25] proposed a methodology to identify areas at risk from spontaneous coal combustion and methane explosions in goafs. The CFD method model tests and the data required to build a numerical model were used. The investigation involved an actual longwall in a hard coal mine that was exploited using a Y ventilation system, which reduces the risk of releasing methane but increases the risk of coal self-ignition. Zhou et al. [29] focused on investigating how curtain setback distance influenced airflow patterns and methane distributions at an empty mining face (no continuous miner present) using full-scale ventilation gallery information gathered from computational fluid dynamics (CFD) models. Hasheminasab et al. [5] analysed the effectiveness of the auxiliary ventilation system on the working coal face section in an underground mine exposed to methane gas. The brattice and exhaust ducted fan make up the auxiliary ventilation system. A computational model is developed, examined, and used in the study using the commercial software program (ANSYS). The numerical simulations provide complete data about the flow field, air velocity, and methane concentration. Krawczyk [11] proposed applying a method for describing train movement through tunnels to the unique geometry of a longwall panel. The finite volume method was used to determine the flow of the air-methane combination. Because the shearer's mobility, moving and deforming meshes were employed to simulate unstable flows.

The difference between the study conducted and the studies already done by other scholars is that the developed numerical model uses real spatial models of the longwall panel standard equipment to capture the airflow resistance along the longwall workings, which was not included in the work [5,25]. The need to formulate complex relationships describing the behaviour of air in contact with underground equipment, as presented in the work [4], was eliminated. A simple mechanism for the methane emission into the longwall workings has been developed without the need to define empirical relationships that require expensive and time-consuming experimental studies, as was presented in the work [7,8]. The results obtained from the CFD model test are

comparable to in-situ observations without the need to use complex numerical grid deformation algorithms to simulate the shearer's movements, as was presented in [11].

The developed numerical method may be helpful through the design and planning stages of both present and future longwall mining with caving, which makes general replication in coal mines feasible.

The geometry of the test object under study maps the Z-11a longwall panel in the 408/1 seam, whose 3D geometry has been prepared in SolidWorks software, while the numerical calculations have been done in SolidWorks Flow Simulation with the use of computational fluid dynamics (CFD) methods.

Materials and methods

The following information was taken into account:

- geometry of the longwall panel (width, height, and angle inclination),
- the geometry of the longwall working, taking into account the geometry of powered roof support, transport equipment, and the longwall shearer,
- geometry of gate roads,
- parameters of goaf (porosity, permeability, and geometry).

The ventilation system of the Z-11a longwall panel was examined to determine the airflow directions. The permeability of goaf was calculated based on the mining and geological conditions of the Z-11a longwall panel.

1.1. The geo-mining conditions of the Z-11a longwall panel

The seam 408/1 reaches a thickness, including overgrowth, of up to about 4.20 metres. The maximum thickness of the overgrowth reaches about 0.60 m, occurs mainly in the roof, and is built up by medium-hard sandy shale. Above this overgrowth is an upper layer of coal about 1.20 metres thick. Below the overgrowth, there are 2-3 layers of coal up to 0.10 m thick, and further on, a layer of coal about 2.20 m thick. The roof contains shale, sandy shale, and sandstone. On the floor of the 408/1 seam, there is shale, sandy shale, and sandstone, and locally, at a distance of 3.0 m, there is a layer of coal about 0.50 m thick. The "U"-type ventilation system was adopted in the Z-11a longwall panel. Fig. 1 shows a map of the longwall panel in the 408/1 seam.

The values of the average compressive strengths (R_c) of the coal of seam 408/1 and the surrounding rocks are:

- the coal of seam 408/1 is 18.8 MPa,
- the floor rocks are 43.57 MPa,
- the roof rocks are 38.1 MPa.

1.2. Geometry

Fig. 2 presents a model of the longwall panel that was investigated. The developed geometry of the model was based on the data in the longwall panel, such as:

- the actual geometry of the shearer,
- the actual geometry of the powered roof supports,

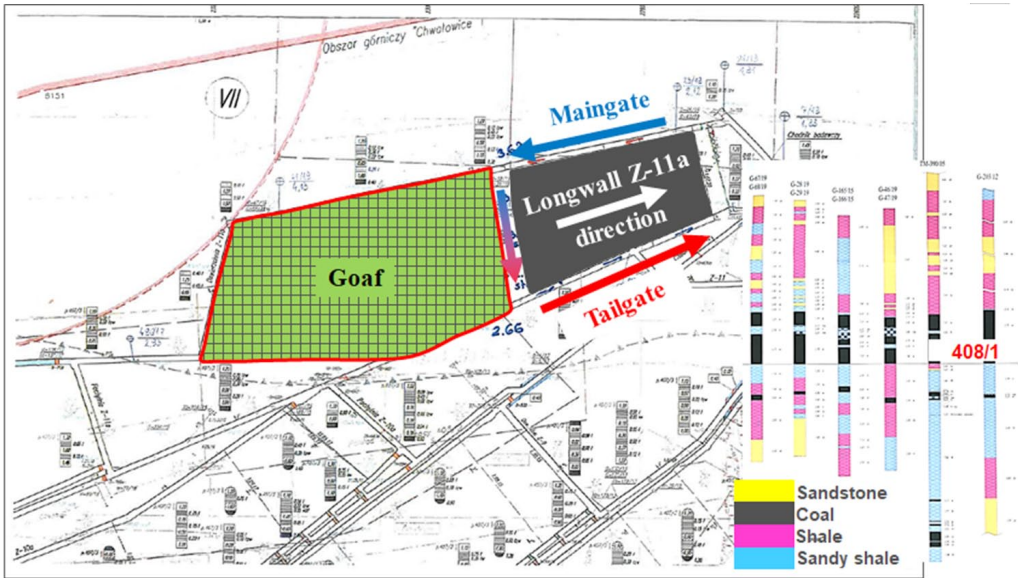


Fig. 1. Geo-mining conditions of Z-11a longwall panel in 408/1 seam

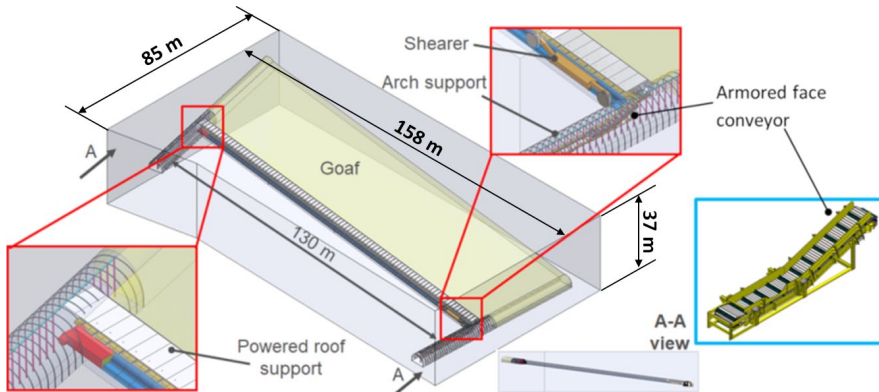


Fig. 2. Geometry of the “U”-type ventilated Z-11a longwall panel

- the actual geometry of the arch supports,
- the actual geometry of the steel props,
- the actual geometry of the armoured face and belt conveyors.

Fig. 3a shows a model of the longwall shearer’s position after the web cut at 32.5 metres. Fig. 3b shows a model of the longwall shearer’s position after the web cut at 65 metres . Fig. 3c shows a model of the longwall shearer’s position after the web cut at a length of 130 metres . The P10/V29/4/A arch support with 1.0 m spacing was used to support the gateroads. The longwall shearer is moving from the top gate to the bottom gate, as shown in Fig. 3.

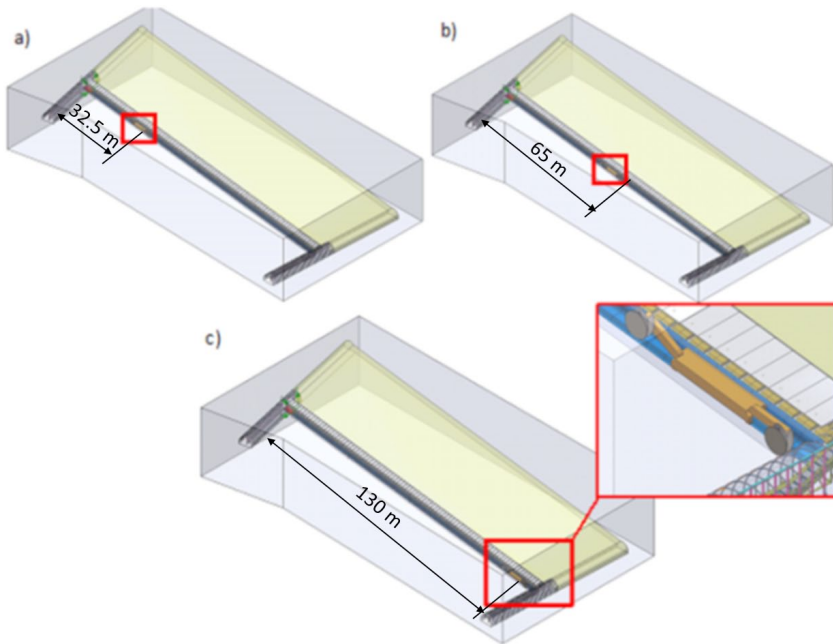


Fig. 3. The longwall shearer position variants: a) variant I; b) variant II; c) variant III

The height of the goaf (Fig. 4) was estimated based on the relationships [1,3,24]:

$$H_{zw} = \frac{100 \cdot h}{c_1 \cdot h + c_2} \quad (1)$$

where [3,24]:

c_1 – a constant depending on the geological structure of the rock mass, (for R_c of rock >40 MPa $c_1 = 2.1$, for R_c of rock $20 \div 40$ MPa $c_1 = 4.7$, for R_c of rock <20 MPa $c_1 = 6.2$),

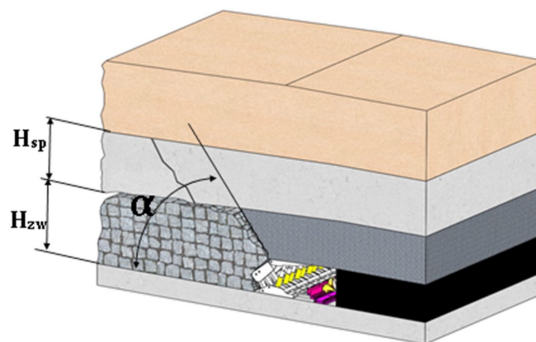


Fig. 4. The height (H_{zw}), the inclination angle (α) and the fracture zone (H_{sp}) of the goaf

c_2 – constant depending on the geological structure of the rock mass, (for R_c of rock >40 MPa $c_2 = 16$, for R_c of rock $20 \div 40$ MPa $c_2 = 19$, for R_c of rock <20 MPa $c_2 = 32$).

The height of the fracture zone (H_{sp}) was calculated by solving the expression given in the form of [1,24]:

$$H_{sp} = \frac{100 \cdot h}{c_3 \cdot h + c_4} \quad (2)$$

where [3,24]:

c_3 – a constant depending on the geological structure of the rock mass, (for R_c of rock >40 MPa $c_3 = 1.2$, for R_c of rock $20 \div 40$ MPa $c_3 = 1.6$, for R_c of rock <20 MPa $c_3 = 3.1$),

c_4 – a constant depending on the geological structure of the rock mass, (for R_c of rocks >40 MPa $c_4 = 2$, for R_c of rocks $20 \div 40$ MPa $c_4 = 3.6$, for R_c of rocks <20 MPa $c_4 = 5$).

Based on the information shown in TABLE 1 [3] and Fig. 5, it is possible to estimate the longwall goaf's angle of inclination.

TABLE 1

Relationship between the inclination angle (α) of the longwall goaf and the average compressive strength (R_c) of roof rocks [3]

Characteristics of roof rocks	Angle of inclination (α)	Compressive strength R_c
	[°]	[MPa]
Extremely weak rocks, including a very weak sandstone	$>81 \div 85^\circ$	<10
Very weak sandstone, weak and soft carbonate shale, very soft and fractured	$>75 \div 81^\circ$	$>10 \div 20$
Most types of shale, sandstone, weak sandstone e.g. moderately stronger, very good rocks	$>65 \div 75^\circ$	$>20 \div 30$
Hard grey shale, medium-strength sandstone	$>50 \div 65^\circ$	$>30 \div 45$
Strong sandstone	$>35 \div 50^\circ$	$>45 \div 60$
Very thick massive sandstone, very strong sandy shale, fine-grained sandstone with shale lamination	$>30 \div 35^\circ$	$>60 \div 80$
Very thick, strong, massive sandstone	$\leq 30^\circ$	>80

From the curve in Fig. 5, it can be concluded that a decrease in the value of the inclination angle of the longwall goaf is accompanied by an increase in the compressive strength of the roof rocks of the longwall working.

The height of the longwall goaf (H_{zw}) can also be estimated using the linear relationship [21,23]:

$$H_{zw} = 3,5 \cdot m_{pw} \quad (3)$$

where: m_{pw} – seam thickness, m.

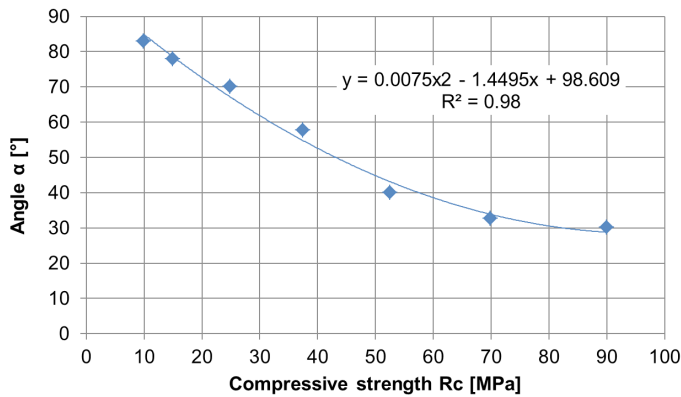


Fig. 5. The inclination angle (α) of the longwall goaf depending on the strength of the roof rock (R_c)

1.3. Numerical grid

A cuboidal orthogonal mesh of finite volumes was used to generate the numerical grid shown in Figs. 6, 7, and 8 for the tested variants. The numerical grid can have a constant size throughout the volume as well as increase its size by a predetermined value defined by refinement level value settings. Reducing the size of the cells and thus increasing the resolution of the numerical grid increases the accuracy of the calculations. Modelling accuracy is the result of approximating the fluid transport equations on shorter grid elements formed from the computational cells [6,7,25]. Throughout the meshing process, colour-coded mesh refinement graphs make it easier to distinguish between stages of refinement and the areas to which they apply.

Numerical grid quality studies were done to ensure that the simulation results were adequate. Fig. 9 shows the analysis's results. At the longwall panel outlet, the volume flow rate was monitored.

TABLE 2 shows the results of the mesh quality investigation.

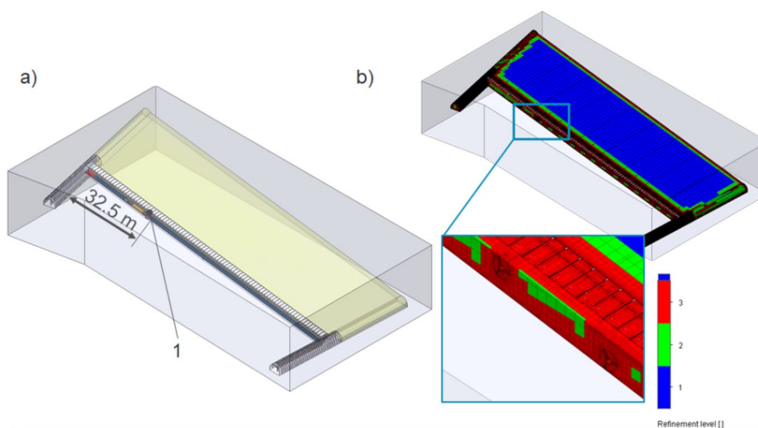


Fig. 6. Numerical grid for variant I of numerical calculations: 1 – shearer position

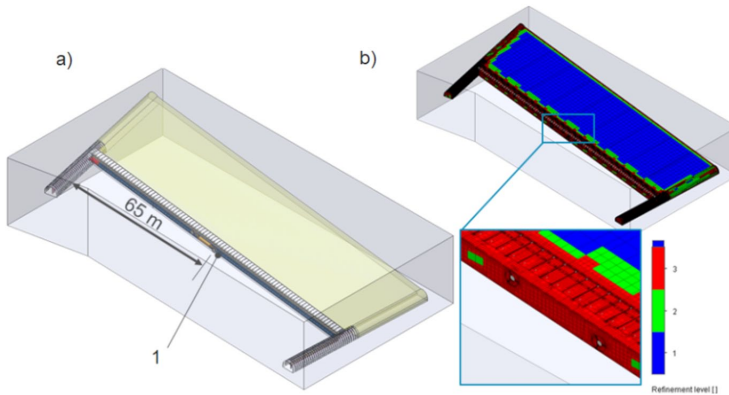


Fig. 7. Numerical grid for variant II of numerical calculations: 1 – shearer position

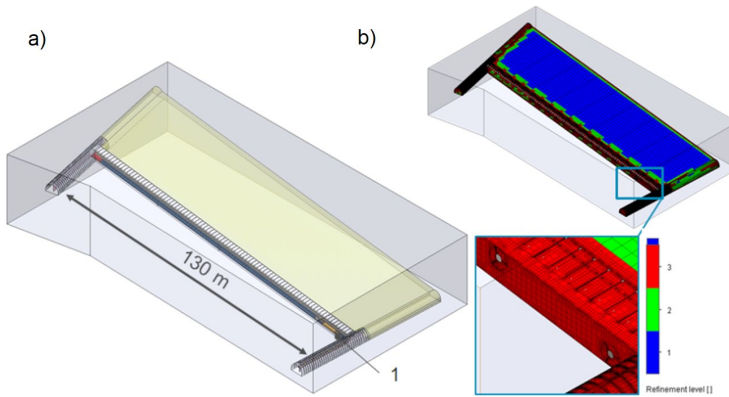


Fig. 8. Numerical grid for variant III of numerical calculations: 1 – shearer position

TABLE 2

Results of the study on the numerical grid's quality

No.	Quality	Total computational cells	Volume flow rate [m^3s^{-1}]
1	coarse mesh	65,716	1288
2	normal mesh	255,428	1294
3	fine mesh	588,312	1298
4	very fine mesh	927,984	1299

The numerical grid will have more than 927,984 total computational cells, as determined by the quality results of a study, as shown in TABLE 2 and Fig. 9.

The numerical grid shown in Figs. 6,7 and 8 satisfies the requirements for accuracy and fidelity of the representation of the fluid geometry, while at the same time allowing a compromise between the accuracy and the number of computational cells. This is a deliberate procedure, applied to dimensionally large three-dimensional objects, as it leads to minimising the time-consuming computation.

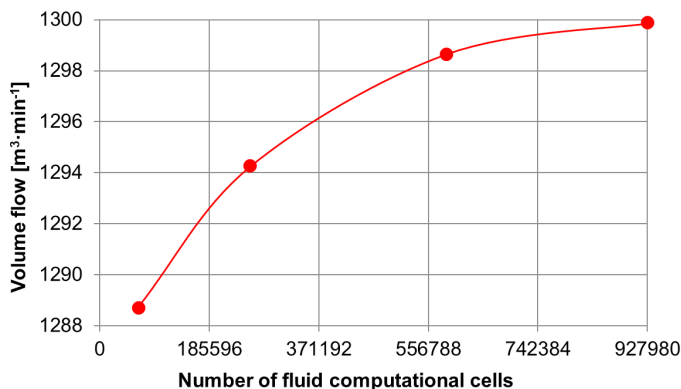


Fig. 9. Numerical grid's quality

1.4. Assumptions

Based on the fluid mechanics and thermodynamic equations, the issue of the flow of the air-methane mixture in the longwall panel is resolved as follows [2,6,25,26]:

mass conservation equation [25,26]:

$$\frac{\partial \rho}{\partial t} + \nabla(\rho \vec{v}) = 0 \quad (4)$$

where:

t – time, s;

ρ – density of the fluid, $\text{kg} \cdot \text{m}^{-3}$;

\vec{v} – velocity of the fluid, $\text{m} \cdot \text{s}^{-1}$;

– Navier-Stokes equation [6]:

$$\rho \frac{\delta \vec{v}}{\delta t} = -\nabla p + \rho \vec{g} + \mu \nabla^2 \vec{v} \quad (5)$$

where:

ρ – density of the fluid, $\text{kg} \cdot \text{m}^{-3}$,

\vec{v} – velocity of the fluid, $\text{m} \cdot \text{s}^{-1}$,

p – pressure, Pa,

\vec{g} – acceleration due to gravity, $\text{m} \cdot \text{s}^{-2}$,

μ – dynamic viscosity of the fluid, $\text{Pa} \cdot \text{s}$.

– energy conservation equation [6]:

$$\frac{\partial}{\partial t}(\rho E) + \nabla[\vec{v}(\rho E + p)] = \nabla[k_{eff} \nabla T - \sum h_j \vec{J}_j + (\vec{\tau}_{eff} \vec{v})] + S_h \quad (6)$$

where:

h – enthalpy, $\text{J} \cdot \text{kg}^{-1}$,

T – temperature, K,

S_h – the energy exchange source, $\text{J} \cdot \text{m}^{-3}$,
 $\tilde{\tau}e_{ff}$ – stress tensor, $\text{kg} \cdot \text{m}^{-3} \cdot \text{s}^{-1}$,
 k_{eff} – conductance coefficient, $\text{W} \cdot \text{m}^{-1} \cdot \text{K}^{-1}$.

Instabilities in the flow of a methane and air mixture through a longwall working and gateroads can cause the turbulent flow phenomenon. The turbulence model μ_t of the flowing fluid was expressed by the following equation [6,26]:

$$\mu_t = \rho C_\mu \frac{k^2}{\varepsilon} \quad (7)$$

The equations express fluid flow for turbulent kinetic energy k and dispersion ε where [2,26]:

– turbulence's kinetic energy represents a solution to the relationship:

$$\frac{\partial \rho k}{\partial t} + \frac{\partial \rho k v_i}{\partial x_i} = \frac{\partial}{\partial x_j} \left[\left(\mu + \frac{\mu_t}{\sigma_k} \right) \frac{\partial k}{\partial x_j} \right] + G_K + G_b - \rho \varepsilon - Y_M + S_k \quad (8)$$

– turbulence's dissipation energy represents a solution to the relationship:

$$\frac{\partial \rho \varepsilon}{\partial t} + \frac{\partial \rho \varepsilon v_i}{\partial x_i} = \frac{\partial}{\partial x_j} \left[\left(\mu + \frac{\mu_t}{\sigma_\varepsilon} \right) \frac{\partial \varepsilon}{\partial x_j} \right] + C_{\varepsilon 1} \frac{\varepsilon}{k} (G_k + C_{\varepsilon 3} G_b) - C_{\varepsilon 2} \rho \frac{\varepsilon^2}{k} + S_\varepsilon \quad (9)$$

where:

- $C_{\varepsilon 1}$ – empirical constant 1,44;
- $C_{\varepsilon 2}$ – empirical constant 1,92;
- $C_{\varepsilon 3}$ – empirical constant;
- C_μ – empirical constant 0,09;
- k – kinetic energy of turbulence, $\text{m}^2 \cdot \text{s}^{-2}$;
- G_k, G_b – turbulence kinetic energy;
- S_k, S_ε – sources;
- t – time, s;
- v_i – velocity vector, $\text{m} \cdot \text{s}^{-1}$;
- Y_M – represents the contribution of the fluctuating dilatation in compressible turbulence to the overall dissipation rate;
- $x_{i,j}$ – coordinates, m;
- ε – rate of dispersion of kinetic energy of turbulence, $\text{m}^2 \cdot \text{s}^{-3}$;
- μ_t – turbulent viscosity, $\text{Pa} \cdot \text{s}$;
- μ – viscosity, $\text{Pa} \cdot \text{s}$;
- σ_k – turbulent Prandtl number of 1,0;
- σ_ε – turbulent Prandtl number of 1,3;
- ρ – density, $\text{kg} \cdot \text{m}^{-3}$.

– thermal equations of state for a gas [6]:

$$p = \rho RT \quad (10)$$

where:

- R – universal gas constant, $\text{J} \cdot \text{kmol}^{-1} \cdot \text{K}^{-1}$;
- T – temperature, K.

1.5. Boundary conditions

As a result of longwall panel extraction, the coal seam is degassed, causing an increase in the concentration of methane in the air. The amount of methane released during coal face mining with a shearer is determined by the amount of coal mined per unit of time as well as its methane-bearing capacity. The estimated methane release during shearer operations in the longwall working allows for calculating the increase in methane concentrations. Methane also flows into the longwall working and goafs as a result of the degassing of the seams laying under and above the longwall panel [12,19-23].

Sources of methane

Fig. 10 shows the sources of the methane streams in the longwall working. Source 1 presents the methane emission rate into the longwall from the coal face. Source 2 depicts the rate of methane emission from the roof and floor as a result of the stress relief of the near coal seams. Source 3 depicts the rate of methane emissions from the goaf [12].

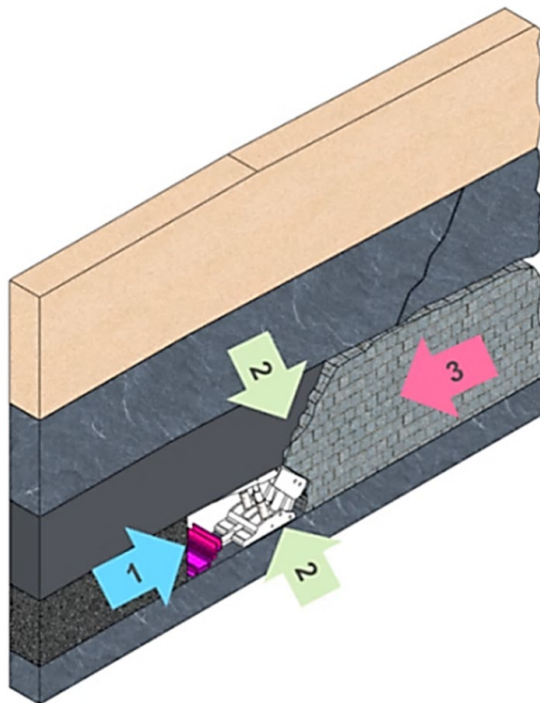


Fig. 10. Sources of methane emission during the longwall mining: 1 – from the coal face, 2 – from the roof and the floor, 3 – from the goaf

The methane emission rate during the web cut of solid coal requires consideration of the geometry of the longwall working, the coal's primary methane-bearing capacity and the time of

the mining cycle. The methane emission rate is directly proportional to the volume of the mined coal, the primary methane-bearing capacity M_o , the degree of degassing η_s and inversely proportional to the time of the mining cycle t and is calculated with the formula [12,13,15,16]:

$$\dot{Q}_S = \frac{L_S m_e \gamma z M_o \eta_s}{100t} \quad (11)$$

where:

- η_s – degree of coal degassing $\eta_s = 8,354 \cdot M_o^{0,67}$, $\text{m}^3 \text{CH}_4 \cdot \text{Mg}_{\text{CSW}}^{-1}$,
- L_S – length, m,
- m_e – height, m,
- γ – density, $\text{Mg} \cdot \text{m}^{-3}$,
- z – web cut, m,
- M_o – methane bearing capacity, $\text{m}^3 \text{CH}_4 \cdot \text{Mg}_{\text{CSW}}^{-1}$,
- η_s – degree of degassing, %,
- t – time, min,
- \dot{Q}_{CH_4} – volume flow of methane during one mining cycle, $\text{m}^3 \text{CH}_4 \cdot \text{min}^{-1}$.

The relationship describing the methane emission rate from near coal seams was calculated using the formula [12]:

$$h_{\min} = 1,73(L_S + L_C) \quad (12)$$

where:

- L_S – width of longwall panel, m,
- L_C – pressure occurrence distance in front of the coal face, m.

The primary methane-bearing capacity M_o was determined according to the relation [12]:

$$M_o = \frac{M_w}{1 - \eta} \quad (13)$$

where:

- M_w – methane-bearing capacity after degassing, $\text{m}^3 \cdot \text{Mg}_{\text{CSW}}^{-1}$,
- η – degassing rate, %.

The amount of methane emission rate from the transported coal to the air was calculated using the relationship [22]:

$$\dot{Q}_u = A(W_c - W_r) \left[1 - \exp\left(-\frac{d}{v_i} x\right) \right] \quad (14)$$

where:

- W_c – total methane content, $\text{m}^3 \text{CH}_4 / \text{Mg}_{\text{CSW}}$,
- W_r – residual methane content, $\text{m}^3 \text{CH}_4 / \text{Mg}_{\text{CSW}}$,
- d – constant of the carbon-methane phase system, $1 \cdot \text{min}^{-1}$,
- v_i – conveyor belt velocity, $\text{m} \cdot \text{min}^{-1}$.

The methane emission rate to the air from the coal face was determined by the following equation [22]:

$$Q_p = q_o \cdot m \cdot b_{ch} \quad (15)$$

where:

q_o – volume flow of methane, $\text{m}^3 \cdot \text{m}^{-2} \cdot \text{min}^{-1}$,

m – coal seam thickness, m,

b_{ch} – width of the longwall working, m.

The influence of the shearer's position during mining on the methane emission rate along a longwall in 60 minutes (3600 seconds) was investigated within the scope of the model tests that were run. The data used in the numerical calculations is shown in TABLE 3.

TABLE 3

Data adopted in numerical calculations

Length of mined coal face L_s	Methane bearing capacity [$\text{m}^3\text{CH}_4/\text{Mg}_{\text{csw}}$]	Degree of degassing during mining [%]	Web cut [m]	Volume flow of methane during coal face mining (predicted)		Methane emissions from the coal face [$\text{m}^3\text{CH}_4/\text{min} \cdot \text{m}$]	Methane emissions from near coal seams [$\text{m}^3\text{CH}_4/\text{min} \cdot \text{m}$]
				t [s]	[$\text{m}^3\text{CH}_4/\text{min}$]		
32.5	2.90	17.05	0.7	1200	2.19	0.163	0.553
65	3.14	17.98		2400	2.50	0.325	1.105
130	3.38	18.89		3600	2.83	0.488	1.658

The web cut in TABLE 3 is the value of the depth of cut on the coal face in the longwall working by the shearer. The coal face is cut in one direction by the shearer. The floor is cleaned, and there is only one sumping operation on the way back. One of the most important variables that enable an accurate assessment of the methane risk and the level of threat from gas and rock outbursts is the so-called methane-bearing capacity, which is the amount of natural methane in hard coal seams. Methane emissions from the coal face are the gas released from the coal broken by the shearer. Methane emissions from near coal seams mean that the gas is released from undermined and overmined coal seams around exploitation by longwall caving at no more than 160 m. The degree of degassing during mining is the factor that describes the degasification percentage degree of roof and floor seams in longwall environments with caving.

Fig. 11 shows the methane emission rate from the coal face to the working of a longwall during the time of the coal face mining. The course of the curve in Fig. 11 was developed based on equation (11) which was adopted in the numerical model as a boundary condition.

The methane-bearing capacity of the coal seam in the Z-11a longwall panel was determined during in-situ measurements. The results of the methane bearing capacity measurements along the longwall working are shown in Fig. 12.

1.5.1. Permeability of the goaf

The principles of goaf modelling are based on the assumption of fluid flow through an immobile granular bed [6,20,21,27,28]. The filtration of goaf is affected by changes in the value

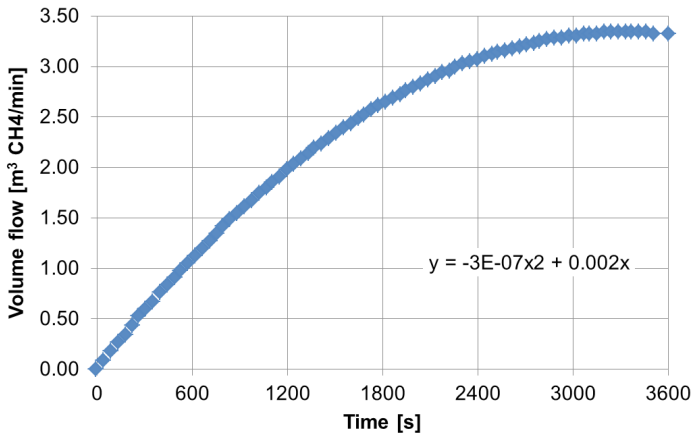


Fig. 11. Methane emission rate from the coal face to the longwall working in time of 3600 seconds

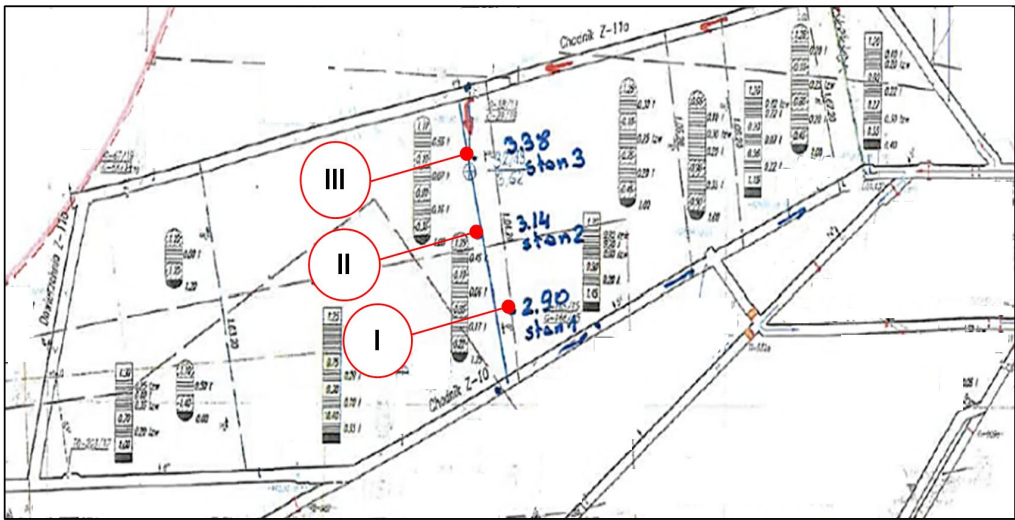


Fig. 12. Methane bearing capacity measurements:
 I – methane bearing capacity measurements for variant I, II – methane bearing capacity measurements for variant II, III – methane bearing capacity measurements for variant III

of distance x measured from the start to the end of the longwall panel. The main parameter characterising the variability of the filtration of goaf is the permeability coefficient k . The permeability coefficient k can be estimated by solving an empirical relationship in the form of [20,21], and [23]:

– for the goaf length variation in the range of 0 to $x \leq 2/3l$ [23]:

$$k = \frac{\mu}{r + ax^2} \tag{16}$$

– for the goaf length variation in the range of $x > 2/3l$ to $x \leq l$ [23]:

$$k = \frac{\mu}{r_0 + a \left(\frac{4}{3}l - x \right)^2} \tag{17}$$

where:

- k – permeability, m,
- x – longwall advance, m,
- l – total length of goaf, m,
- μ – dynamic viscosity, Pa · s,
- r_0, a – factor depending on mining and geological conditions.

The permeability of goaf was illustrated in Figs. 13÷14. The figures are based on the assumption that the longwall goaf length is 1,000 metres and that the roof rocks of the longwall working are sandstone and shale. The red line on the graph expresses the variation of the permeability of

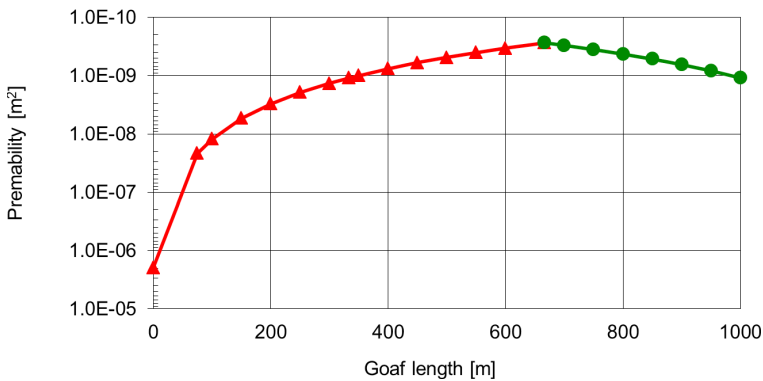


Fig. 13. The permeability of goaf formed from a shale

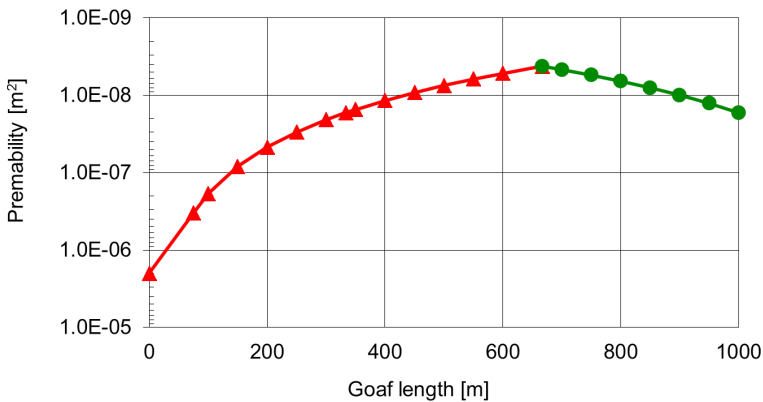


Fig. 14. The permeability of goaf formed from a sandstone

the goaf according to the relationship (16). The green line illustrates the variation in the value of the permeability of the leaf according to the relationship (17).

From the curve formation in Figs. 13÷14, it can be observed that the maximum values of the permeability coefficient k occur near the longwall working, while at a distance of about 2/3 from the longwall working, this parameter reaches its minimum values. In the distance between 650 and 1,000 metres, an increase in the permeability of the goaf can be observed.

The goaf filtering capacity was estimated in accordance with the relationship [27,28]:

$$Q = kA_o \frac{\rho \hat{g} \cdot P}{\eta H} \quad (18)$$

where:

- H – height, m,
- Δp – pressure drop, Pa,
- A_o – cross-section, m^2 ,
- d_p – diameter, m,
- η – viscosity, $N \cdot s \cdot m^{-2}$.

The relationship interpreted by equation (18) is an extension of Darcy's law [6,27,28].

The following boundary conditions were adopted for the analysed issue:

- the volume flow of air: $1300 \text{ m}^3 \cdot \text{min}^{-1}$,
- the average porosity of the goaf: 30% [8],
- the gravity: $9.81 \text{ m} \cdot \text{s}^{-2}$,
- the average temperature of the air: 32°C ,
- the longwall working length: 130 m,
- the longwall working height: 2.9 m
- the goaf height: 10.15 m,
- the methane emission rate: according to Table 3,
- coal seam degassing degree: according to Table 3,
- the web cut: 0.7 m,
- the density of coal: $1.3 \text{ Mg} \cdot \text{m}^{-3}$,
- the initial methane concentration in the air: 0.1%,
- the methane bearing capacity of coal seam: according to Table 3,
- the average inclination angle of the goaf: 55° ,
- the average relative humidity of air: 80%,
- the air pressure: 97800 Pa,
- the specific heat ratio of oxygen (C_p/C_v): 1.39472,
- the specific heat ratio of nitrogen (C_p/C_v): 1.3996,
- the specific heat ratio of methane (C_p/C_v): 1.30458,
- the average dynamic viscosity of oxygen: $2.05 \cdot 10^{-5} \text{ Pa} \cdot \text{s}$,
- the average dynamic viscosity of nitrogen: $1.78 \cdot 10^{-5} \text{ Pa} \cdot \text{s}$,
- the average dynamic viscosity of methane: $1.108 \cdot 10^{-5} \text{ Pa} \cdot \text{s}$,
- the average thermal conductivity of oxygen: $0.027276 \text{ W} \cdot \text{m}^{-1} \cdot \text{K}^{-1}$,
- the average thermal conductivity of nitrogen: $0.0259 \text{ W} \cdot \text{m}^{-1} \cdot \text{K}^{-1}$,
- the average thermal conductivity of methane: $0.03540 \text{ W} \cdot \text{m}^{-1} \cdot \text{K}^{-1}$,
- cross section of gateroads according to arch support ŁP10/V29/4/A geometry.

2. Results

Figs. 15-17 presents the results of the numerical calculations for each variant separately. A map of the methane distribution for variation I of the numerical solution is shown in Fig. 15. A map of the methane distribution for variation II is shown in Fig. 16. A map of the methane distribution for variation III of the numerical solution is shown in Fig. 17.

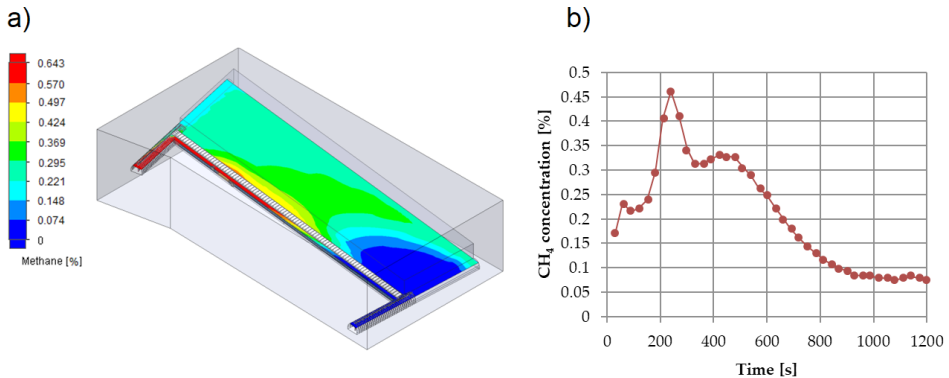


Fig. 15. Methane distribution for variant I at a time interval of 1200 seconds:
 a) A methane distribution map; b) A methane distribution at the longwall panel outlet

The maximum value of methane concentration was 0.46% at 240 seconds, as shown in Fig. 15. The methane concentration decreased to a value of 0.08% at 1200 seconds, after 240 seconds.

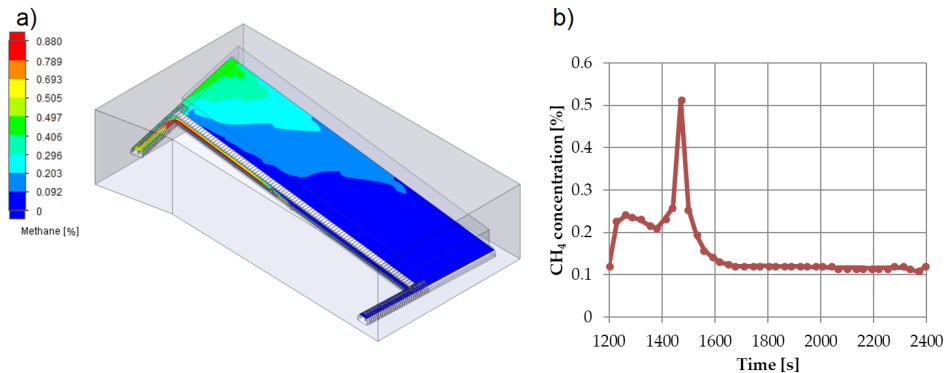


Fig. 16. Methane distribution for variant II at a time interval of 1200 to 2400 seconds:
 a) A methane distribution map; b) A methane distribution at the longwall panel outlet

The maximum value of methane concentration was 0.51% at 1470 seconds, as shown in Fig. 16. The methane concentration decreased to a value of 0.12% at 2400 seconds, after 1470 seconds.

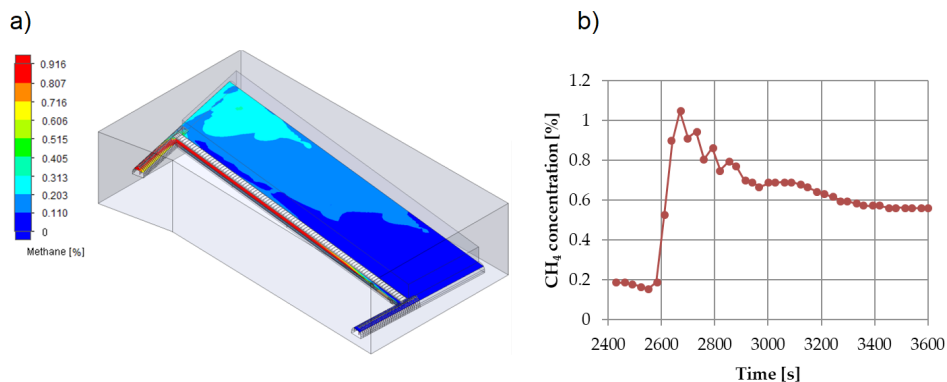


Fig. 17. Methane distribution for variant III at a time interval of 2400 to 3600 seconds: a) A methane distribution map; b) A methane distribution at the longwall panel outlet

The maximum value of methane concentration was 1.04% at 2670 seconds, as shown in Fig. 17. The methane concentration decreased to 0.55% at 3600 seconds, after 2670 seconds.

Fig. 18 compares the results of methane concentration changes determined by in-situ measurements and numerical computations during 3600 seconds. The maximum values of methane concentration are represented in Fig. 18 by the symbols P1, P2, and P3. Methane-monitoring systems for coal mining applications were used to measure the amount of methane in the air.

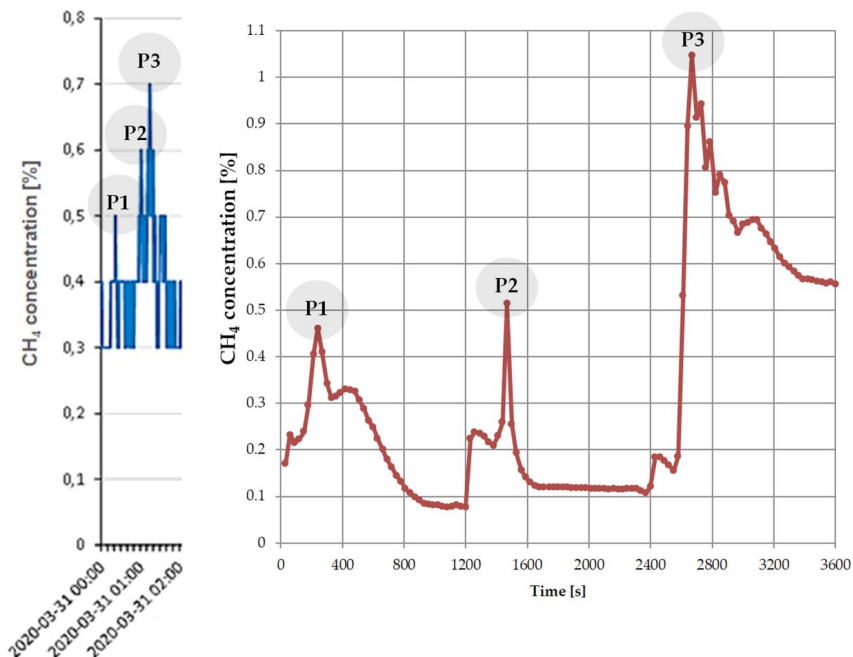


Fig. 18. Results of the model tests: a) in-situ, b) CFD

The maximum methane concentration values under in-situ conditions are: 0.5% CH₄ for the first 1200 seconds, 0.6% CH₄ for the second 2400 seconds, and 0.70% CH₄ for the last 3600 seconds. In the case of the numerical calculations, the maximum methane concentration values are 0.46% CH₄ for the first 1200 seconds, 0.51% CH₄ for the first 2400 seconds, and 1.04% CH₄ for the last 3600 seconds. The results obtained from the in-situ measurements and the numerical calculations were compared in TABLE 4.

TABLE 4

Comparison of the results

No.	In-situ measurement, CH ₄ [%]	Numerical model CFD, CH ₄ [%]
1	0.50	0.46
2	0.60	0.51
3	0.70	1.04

3. Conclusions

The interpretation of modelling results should be subjected to a critical assessment of correctness relative to the actual course of the phenomenon. The results of the qualitative and quantitative analysis in the form of effective animations, charts, or colour maps, may be subject to errors due to the assumptions made at the modelling stage. The modelling of methane emissions in the longwall panels is a reflection of our knowledge of the processes taking place. It is important to obtain a correspondence between the modelled phenomenon and in-situ observations.

The results of the model tests and in-situ observations allow for the formulation of the following conclusions:

- the agreement of the results of in-situ measurements with the results of numerical calculations confirms the correctness of the assemblies adopted for the developed CFD numerical model,
- the in-situ observations and numerical simulations show that the longwall shearer's control parameters impact methane concentration changes in the longwall working,
- the presented methodology for methane emission prediction based on CFD methods may be useful in the design stage of longwall panel operations,
- the proposed numerical model offers the ability to forecast the methane concentration distribution based on the position of the shearer,
- the developed methodology and model may be helpful for evaluations that include multiple longwall mining phases in addition to varied shearer's locations,
- the results of the developed numerical model might be helpful while designing underground mining. They can resolve several problems that can arise while mining.

Acknowledgment

The study was carried out as part of the PICTO research project titled "Production Face Environmental Risk Minimization in Coal and Lignite Mines", No. 800711, financed by the Research Programme of the Research Fund for Coal and Steel (RFCS) and Polish MNiSW w93/FBWiS/2018.

References

- [1] M. Bai, F.S.Kendorski, D.J. Van Roosendaal, Chinese and North American high-extraction underground coal mining strata behaviour and water protection experience and guidelines. In Proceedings of the 14th International Conference on Ground Control in Mining, Morgantown, WV, USA, 1-3 August (1995).
- [2] G. Daloğlu, M. Önder, T. Parra, Modelling of Methane and Air Velocity Behavior in an Auxiliary Ventilated Coal Heading. *Arch. Min. Sci.* **66** (1), 69-84 (2021).
- [3] S.K. Das, Observations and classification of roof strata behaviour over longwall coal mining panels in India. *International Journal of Rock Mechanics and Mining Sciences* **37**, 585-597 (2000).
- [4] W. Dziurzyński, A. Krach, J. Krawczyk, T. Pałka, Numerical Simulation of Shearer Operation in a Longwall District. *Energies* **13**, 5559, 1-13 (2020). DOI: <https://doi.org/10.3390/en13215559>
- [5] F. Hasheminasab, R. Bagherpour, S.M. Aminossadati, Numerical simulation of methane distribution in development zones of underground coal mines equipped with auxiliary ventilation. *Tunnelling and Underground Space Technology* **89**, 68-77 (2019).
- [6] Z. Jaworski (Ed.), *Numeryczna mechanika płynów w inżynierii chemicznej i procesowej*. Akademicka Oficyna Wydawnicza EXIT, Warszawa 2005.
- [7] J. Janus, J. Krawczyk, Modelowanie przepływu powietrza w narożu ściany wydobywczej. *Prace Instytutu Mechaniki Górotworu PAN* **1-4** (22), 9-16 (2020).
- [8] A. Juganda, C. Strebinger, J.F. Brune, G.E. Bogin, Discrete modelling of a longwall coal mine gob for CFD simulation. *International Journal of Mining Science and Technology* **4** (30), 463-469 (2020).
- [9] A. Juganda, C. Strebinger, J.F. Brune et al., Computational Fluid Dynamics Modeling of a Methane Gas Explosion in a Full-Scale, Underground Longwall Coal Mine. *Mining, Metallurgy & Exploration* **39**, 897-916 (2022). DOI: <https://doi.org/10.1007/s42461-022-00587-z>
- [10] H. Koptoń, Impact assessment of sorption properties of coal on methane emissions into longwall working. *Arch. Min. Sci.* **65** (3), 605-625 (2020).
- [11] J. Krawczyk, A preliminary study on selected methods of modelling the effect of shearer operation on methane propagation and ventilation at longwalls. *Int. J. Min. Sci. Technol.* **30**, 675-682 (2020).
- [12] E. Krause, Profilaktyka w pokładach metanowych zagrożonych sejsmicznie. *Prace Naukowe GIG, Górnictwo i Środowisko* (3), 65-79 (2005).
- [13] E. Krause, W. Dziurzyński, Projektowanie eksploatacji pokładów węgla kamiennego w warunkach skojarzonego zagrożenia metanowo – pożarowego. GIG, Katowice 2015.
- [14] E. Krause, A. Przystolik, B. Jura, Warunki bezpieczeństwa wentylacyjno-metanowego w ścianach o wysokiej koncentracji wydobywania. XXI Międzynarodowa Konferencja Naukowo-techniczna Górnictwo i Zagrożenia Naturalne. 6-8.11.2019 r., Jawor k. Bielska Białej.
- [15] E. Krause, Z. Lubosik, Wpływ koncentracji wydobywania podczas eksploatacji pokładów silnie metanowych na wydzielanie się metanu do środowiska ścian. 9th International Symposium on Occupational Heat and Safety Petrosani Rumunia. October 3rd 2019 r.
- [16] E. Krause, J. Skiba, B. Jura, Overview of Ventilation Characteristic, Practices and regulations in Poland. XXVIII Szkoła Eksploatacji Podziemnej, Kraków, 25-27.02.2019 r.
- [17] E. Krause, B. Jura, J. Skiba, Mining speed control in the coal panel with high coal output concentration. Kontrola prędkości urabiania w ścianach o wysokiej koncentracji wydobywania. Spotkanie Grupy Roboczej Ekspertów ds. metanu z kopalń Europejskiej Komisji Gospodarczej ONZ. Genewa 7-8.11.2019 r.
- [18] P.M.V. Nguyen, A. Walentek, K. Wierzbński, M. Zmarły, Prediction of the Absolute Methane Emission Rate for Longwall Caving Extraction Based on Rock Mass Modelling – A Case Study. *Energies* **15**, 4958 (2022). DOI: <https://doi.org/10.3390/en15144958>
- [19] N. Szlązak, J. Szlązak, Wentylacja wyrobisk ścianowych w kopalniach węgla kamiennego, w warunkach zagrożenia metanowego i pożarowego. *Górnictwo i Geologia* **8**, 2 (2019).
- [20] N. Szlązak, J. Szlązak, Badania numeryczne i kopalniane przepływu powietrza przez zroby ścian zawałowych. *Górnictwo i Geoinżynieria* **28**, 3, 59-78 (2004).

- [21] J. Szlązak, N. Szlązak, Filtracja powietrza przez zroby ścian zawałowych w kopalniach węgla kamiennego. Wydawnictwa Naukowe AGH Kraków 2005.
- [22] N. Szlązak, M. Borowski, Badania wydzielania metanu do wyrobiska chodnikowych drażonych kombajnami w pokładach węgla. *Górnictwo i Geoinżynieria* **30**, 1, 45-55 (2006).
- [23] L. Świerczek, Wpływ prędkości powietrza przepływającego przez ścianę na przewietrzanie zrobów zawałowych i profilaktykę pożarową. *Przegląd Górniczy* **72**, 2, 34-43 (2016).
- [24] K. Tajduś, A. Tajduś, Określenie wartości parametrów odkształceniowych górotworu poddanego wpływow eksploatacji górniczej na przykładzie KWK „Ziemowit”. *Przegląd Górniczy* **66**, 7-8, 1-6 (2010).
- [25] M. Tutak, J. Brodny and G. Galecki, Applying CFD Model Studies to Determine Zones at Risk of Methane Explosion and Spontaneous Combustion of Coal in Goaves. *Acta Montanistica Slovaca* **27**, (3) 651-666 (2022).
- [26] A. Walentek, T. Janoszek, S. Prusek, A. Wrana, Influence of longwall gateroad convergence on the process of mine ventilation network-model tests. *International Journal of Mining Science and Technology* **4**, 29, 585-590 (2019).
- [27] G. Wałowski, G. Filipczak, Ocena hydrodynamiki przepływu gazu przez ośrodek szczelinowo-porowaty. *Inż. Ap. Chem.* **52**, 6, 581-582 (2013).
- [28] G. Wałowski, G. Filipczak, Gazoprzepuszczalność materiałów porowatych o anizotropowej strukturze. *Inż. Ap. Chem.* **55**, 6, 245-250 (2016).
- [29] L. Zhou, C. Pritchard, Y. Zheng, CFD modelling of methane distribution at a continuous miner face with various curtain setback distances. *Int. J. Min. Sci. Technol.* **25** (4), 635-640 (2015).